Journal of Glaciology

Article

Cite this article: Yang R, Hock R, Kang S, Shangguan D, Guo W (2020). Glacier mass and area changes on the Kenai Peninsula, Alaska, 1986–2016. *Journal of Glaciology* **66**(258), 603–617. https://doi.org/10.1017/jog.2020.32

Received: 5 August 2019
Revised: 8 April 2020
Accepted: 8 April 2020
First published online: 5 May 2020

Key words:
Alaska; climate change; glacier; Kenai Peninsula; mass balance; remote sensing

Author for correspondence:
Wanqin Guo, E-mail: guowq@lzb.ac.cn

cambridge.org/jog

Glacier mass and area changes on the Kenai Peninsula, Alaska, 1986–2016

Ruitang Yang[1,2,4], Regine Hock[2], Shichang Kang[1,3,4], Donghui Shangguan[1] and Wanqin Guo[1]

[1]State Key Laboratory of Cryospheric Science, Northwest Institute of Eco-Environment and Resources, Chinese Academy of Sciences, Lanzhou 730000, China; [2]Geophysical Institute, University of Alaska Fairbanks, Fairbanks, AK, USA; [3]CAS Center for Excellence in Tibetan Plateau Earth Sciences, Chinese Academy of Sciences, Beijing 100101, China and [4]University of Chinese Academy of Sciences, Beijing 100049, China

Abstract

Glacier mass loss in Alaska has implications for global sea level rise, fresh water input into the Gulf of Alaska and terrestrial fresh water resources. We map all glaciers (>4000 km^2) on the Kenai Peninsula, south central Alaska, for the years 1986, 1995, 2005 and 2016, using satellite images. Changes in surface elevation and volume are determined by differencing a digital elevation model (DEM) derived from Advanced Spaceborne Thermal Emission and Reflection Radiometer stereo images in 2005 from the Interferometric Synthetic Aperture Radar DEM of 2014. The glacier area shrunk by 543 ± 123 km^2 (12 ± 3%) between 1986 and 2016. The region-wide mass-balance rate between 2005 and 2014 was −0.94 ± 0.12 m w.e. a^{-1} (−3.84 ± 0.50 Gt a^{-1}), which is almost twice as negative than found for earlier periods in previous studies indicating an acceleration in glacier mass loss in this region. Area-averaged mass changes were most negative for lake-terminating glaciers (−1.37 ± 0.13 m w.e. a^{-1}), followed by land-terminating glaciers (−1.02 ± 0.13 m w.e. a^{-1}) and tidewater glaciers (−0.45 ± 0.14 m w.e. a^{-1}). Unambiguous attribution of the observed acceleration in mass loss over the last decades is hampered by the scarcity of observational data, especially at high elevation, and by large interannual variability.

1. Introduction

Alaskan glaciers account for ~12% of the total global glacierized area excluding the Greenland and Antarctica ice sheets (Pfeffer and others, 2014; RGI Consortium, 2017) and are an important contributor to global sea level rise (Dyurgerov and Meier, 1997; Arendt and others, 2002, 2013; Meier and Dyurgerov, 2002; Berthier and others, 2010; Arendt, 2011; Gardner and others, 2013; Larsen and others, 2015; Zemp and others, 2019). Gardner and others (2013) found a mass change of −50 ± 17 Gt a^{-1} for the period 2003–2009 for all glaciers in Alaska and adjacent Yukon Territory. Subsequent estimates based on gravimetric methods (Wouters and others, 2019), glaciological and geodetic measurements (Zemp and others, 2019) and a combination of these methods (Box and others, 2018) vary between −48 ± 9 and −73 ± 17 Gt a^{-1} for the period 2006–2016. Johnson and others (2013) found highly variable mass change rates for the glaciers in the Glacier Bay region (~6400 km^2) during the period 1995 and 2011 with no clear trend, while Das and others (2014) found a decrease in mass balance of all glaciers in the Wrangell Mountains (~5000 km^2) from −0.07 ± 0.19 m water equivalent (w.e.) a^{-1} in 1957–2000 to −0.24 ± 0.16 m w.e. a^{-1} in 2000–2007 although uncertainty ranges overlap. Wastlhuber and others (2017) found accelerated elevation change for the glaciers (~700 km^2) in the Susitna River basin (−0.14 ± 0.07 m a^{-1} in 1951–2005 compared to −1.20 ± 0.75 m a^{-1} in 2005–2010). Also, all five benchmark glaciers in Alaska (Gulkana, Wolverine, Lemon Creek, South Cascade and Sperry Glacier) have lost mass with average mass-balance rates ranging from −0.58 to −0.30 m w.e. a^{-1} since mid-20th century (O'Neel and others, 2014; O'Neel and others, 2019).

Several studies report on glacier changes on the Kenai Peninsula in south-central Alaska. An early study showed that glaciers in this region have experienced widespread recession since the Little Ice Age Maximum (late 1700s through late 1800s) (Wiles and Calkin, 1992). Most studies on Kenai glaciers have been carried out on parts of the whole glacierized region. Aðalgeirsdóttir and others (1998) studied the volume change of Harding Icefield (subregion II in Fig. 1) through comparing the United Stations Geological Survey (USGS) topography maps in the 1950s and airborne Lidar elevations along center-lines in 1994/1996, and found the Harding Icefield had lost ~34 km^3 of its total volume, corresponding to an area averaged elevation change of −21 m over the ~43 years. Another study using Landsat images shows that the Harding Icefield and Grewingk-Yalik Glacier Complex (subregions I and II, Fig. 1) lost ~78 km^2 (~3.6%) of their glacier area between 1986 and 2002 (Hall and others, 2005). A comparison between USGS maps (1950) and SRTM DEMs also indicates that glaciers in the same region (subregions I and II) were thinning at a rate of 0.61 ± 0.12 m a^{-1} for the period 1950–1999, and the thinning rate for Harding Icefield had further accelerated by a factor of 1.5 during the mid-1990s–1999 relative to 1950 to the mid-1990s (VanLooy and others, 2006).

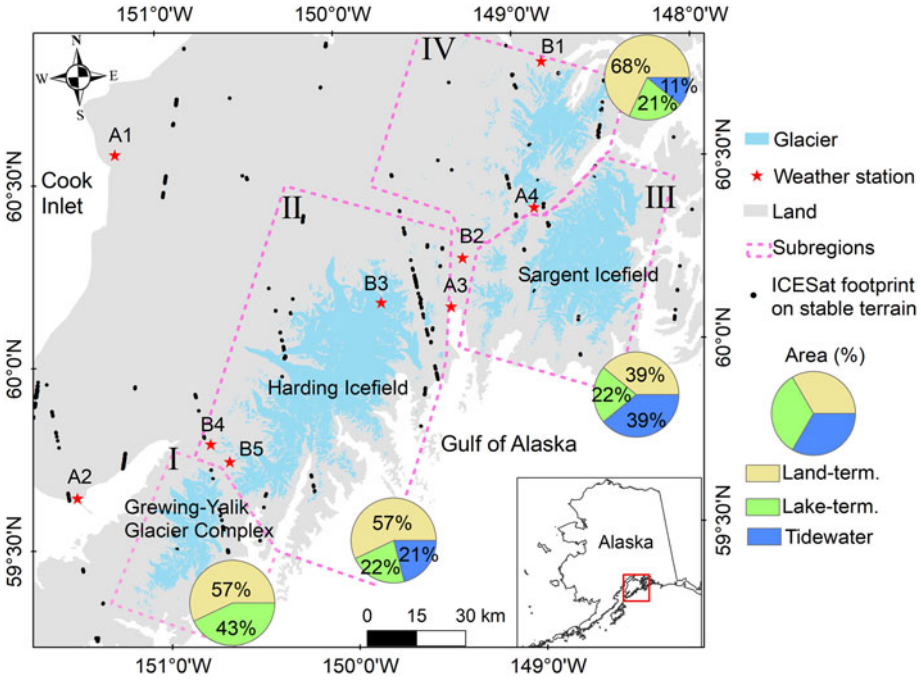

Fig. 1. Map of studied glaciers on the Kenai Peninsula. Black dots show the ICES at footprint on stable terrain (i.e. terrain without glacier, water and vegetation), while red stars refer to weather stations (Table S1). The dashed polygons refer to four subregions analyzed separately in this study. The pie charts show the regional fraction covered by land-terminating, lake-terminating and tidewater glaciers.

This study aims to quantify recent area and mass changes of all glaciers on the Kenai Peninsula aggregated in four subregions defined by the major icefields of the peninsula. First, we compile four new glacier inventories based on multiple satellite images for the years 1986, 1995, 2005 and 2016, which are more comprehensive and detailed than those used in previous studies (Hall and others, 2005; VanLooy and others, 2006; Le Bris and others, 2011; Kienholz and others, 2015). Second, from these inventories we assess the glacier area changes. Finally, we determine the glacier volume and mass changes between 2005 and 2014 using DEMs derived from satellite imagery.

2. Study area

The Kenai Peninsula is located in south-central Alaska, between the Cook Inlet and the Gulf of Alaska (Fig. 1). The Kenai Mountains are an effective barrier for wet airflow (Le Bris and others, 2011), resulting in frequent cloud cover, and high precipitation on the windward south-eastern side of the mountains, while the leeward side lies in the rain shadow. Hence, the glaciers experience a predominantly maritime climate along the south and east side of the peninsula, while a more continental climate prevails in the northern and western parts. The annual total precipitation at a weather station located in the northeast (station A3, Fig. 1) is ~1800 mm, while stations A1 and A2 on the west coast of the Peninsula receive annual totals of ~600 and ~500 mm, respectively, averaged over the period 1986–2016 (https://gis.ncdc.noaa.gov/maps/ncei/summaries/monthly, Table S1).

There are ~1460 glaciers on the Kenai Peninsula, spanning from sea level to ~2000 m a.s.l. and covering 4165 km^2, which corresponds to ~5% of the total glacierized area in Alaska according to the Randolph Glacier Inventory (RGI 6.0; RGI Consortium, 2017). Of all glaciers, only 11 are tidewater and 14 are lake-terminating, but they cover 948 km^2 (22.7% of total area) and 968 km^2 (23.2%), respectively. The Sargent and Harding icefields are the largest ice masses. Especially the Harding icefield has been the focus of several glaciological studies (Aðalgeirsdóttir and others, 1998; Hall and others, 2005; VanLooy and others, 2006).

3. Data and methods

3.1 Glacier outlines extraction and attributes calculation

We used data from Landsat complemented by Sentinel-2 and ASTER images (Table S2), where Landsat data were not available or relevant parts of the Landsat scenes were too cloudy or snowy to extract glacier outlines with sufficient accuracy to compute area changes. A total of 12 orthorectified satellite scenes acquired at the end of the ablation season (04 August to 26 September) were used to delineate glacier outlines for the years 1986, 1995, 2005 and 2016 (Fig. S1). Only images with minimum cloud cover and seasonal snow were chosen. All images (Table S2) were retrieved from the USGS (https://glovis.usgs.gov).

The glacier outlines for clean ice were delineated using a semi-automatic procedure based on the band ratio segmentation method (Paul, 2000; Albert, 2002; Guo and others, 2015; Li and others, 2017). A red/short-wave infrared (R/SWIR) band ratio with a threshold of 2–2.5 (TM3/TM5 of Landsat TM and ETM+, TM4/TM6 of Landsat OLI imagery) and an additional threshold on the blue band (band 1 of TM/ETM+ and band 2 of OLI) digital number were adopted and thresholds were selected interactively (Paul and Kääb, 2005; Raup and others, 2007). We employed sectionalized glacier outline delineation by using moving windows with different optimal band ratio thresholds on the same satellite image to minimize the influence of various snow/ice ablation levels on the optimal thresholds (Guo and others, 2015). We also applied a median filter (3 by 3 kernel) to reduce noise in shadowed regions and remove isolated pixels outside the glaciers, although it might reduce the size of small glaciers to some extent (Paul, 2002; Andreassen and others, 2008). Only glaciers with an area ≥0.01 km^2 were mapped. Following previous studies (Hall and others, 1992; Racoviteanu and others, 2008*a*; Pan and others, 2012; Burns and Nolin, 2014), debris-covered glacier margins were delineated manually from visual inspection of the images. Clean ice outlines were visually inspected using all available contrast-enhanced false-color composite images as well as Google Earth^{TM} images to correct errors caused by cast shadow, light clouds and seasonal snow.

Following the top-down method (Guo and others, 2015), which identifies the ice divides by aspect differences between

https://doi.org/10.1017/jog.2020.32 Published online by Cambridge University Press

the two sides of mountain ridges, we derived ice divides by using the IFSAR DEM, within a 1500 m buffer distance from all glaciers. Results were scrutinized with the help of the shaded relief data and the Landsat scenes, while gross errors were corrected manually where necessary. The ice divides were used to split the glacier complex into individual glaciers.

We extracted a series of glacier-specific attributes including Global Land Ice Measurements from Space (GLIMS)-IDs, coordinates, surface area, debris-covered area, mean slope and aspect, maximum, mean and minimum elevation using the IFSAR DEM and glacier outlines, and added glacier names (if existing) and glacier terminate types (land-terminating, lake-terminating and tidewater) from RGI 6.0. Mean aspect was derived from the arctangent of the mean values of the sine and cosine of the aspect of all DEM cells within a glacier.

3.2 DEM generation and mass change derivation

DEMs derived from ASTER L1A stereo images in 2005 (Fig. 1) and the IFSAR DEM in 2014, were used to compute surface elevation and glacier volume changes over the period 2005–2014. The ASTER data were acquired between 9 August and 14 August, while the IFSAR data were acquired between 29 August and 12 September 2014 (http://viewer.nationalmap.gov/basic/ access date: December 2018, Table S3).

3.2.1 IFSAR DEM and validation

As part of the Alaska Statewide Digital Mapping Initiative, which started in 2010, the IFSAR DEM was acquired from airborne radar operating in the X- and P- bands, with a native resolution of 5 m mosaics. In this study, we used the elevation data product, IFSAR Digital Surface Model (DSM), which is based only on the X-band, since the X-band signal generally penetrates the glacier surface less deep than the P-band (Bert and others, 2011). X-band radar (9.7 GHz) has been shown to penetrate snow and ice (e.g. Rignot and others, 2001; Gardelle and others, 2012; Gusmeroli and others, 2013) depending on the grain size and surface wetness (Mätzler and Schanda, 1984), as well as frequency (Davis and Poznyak, 1993; McNabb and others, 2019). X-band penetration depths are not well known, but in cold and dry snow penetration depths of several meters have been found in Antarctica (Davis and Poznyak, 1993; Surdyk, 2002) and at high elevations in the European Alps (Millan and others, 2015; Dehecq and others, 2016). Some geodetic mass-balance studies have therefore applied multi-meter corrections to account for radar penetration (e.g. Melkonian and others, 2014; Round and others, 2017; Lambrecht and others, 2018). However, over wet glacier surfaces radar penetration is limited to a few centimeters below the surface (Mätzler and Schanda, 1984).

To estimate surface wetness, we analyze air temperature records from three weather stations at high elevation (990–1420 m a.s.l.) on or close to the ice cap during and preceding the period of IFSAR acquisition (Fig. S2). Daily mean and minimum air temperatures were generally well above 0°C leading us to conclude that meltwater was present at or immediately below the surface during this period. Hence, we assume radar penetration to be negligible in this study.

Elevation data derived from Ice, Cloud and Land Elevation Satellite Geoscience Laser Altimeter System (ICESat/GlAS) laser altimeter were used to validate the IFSAR DEM. We used the data from GLAH14 (release 634), available from the National Snow and Ice Data Center (NSIDC). The data has a 10.6 ± 4.5 m horizontal and 0.34 m vertical accuracy (Magruder and others, 2007), and is considered to be the most consistent globally available elevation data (Zwally and others, 2014). To minimize the influence of land surface changes, we only compared the IFSAR and GLAH14 data over stable terrain, i.e. we excluded all glacier, lake, ocean and vegetation pixels as extracted from the land cover map of Alaska (USGS, 2011, https://gapanalysis.usgs.gov/gaplandcover/data/download/).

The Ellipsoid of the ICESat data was first transformed from TOPEX/Poseidon Ellipsoid to WGS84 Ellipsoid and then to NAD83, while the vertical datum was transferred from WGS84 to NAVD88 (same as IFSAR DEM) through an online tool (https://vdatum.noaa.gov/vdatumweb/). For each ICESat footprint, the corresponding IFSAR elevation was extracted by calculating the area-weighted average of the elevations of all pixels fully or partially enclosed by a circle with 35 m radius around the footprint's center (Brun and others, 2017). ICESat/GLAS data with slope larger than 5° were omitted (VanLooy and others, 2006; Le Bris and Paul, 2015), and outliers were removed based on the 'Interquartile range'(IQR), where only data between $Q_1 - 1.5 \cdot IQR$ and $Q_3 + 1.5 \cdot IQR$ were used (Q_1 is the middle value in the first half of the rank-ordered dataset; Q_3 is the middle value in the second half of the rank-ordered dataset), and the rest discarded as outliers (McGill and others, 1978). The mean and Std dev. of the elevation differences between ICESat data and IFSAR DEM is 0.53 ± 1.38 m, indicating reasonable agreement between the two data sets. For comparison differences between the IFSAR and ICESat/GLAS data for slopes larger than 5° are shown in Table S4.

3.2.2 Derivation of ASTER DEMs and bias corrections

The ASTER DEMs were generated from ASTER L1A stereo images (3N and 3B bands) in early August 2005, using the DEM Extraction Wizard of ENVI 5.1 with the geographic reference system NAD83 UTM subregion 5N or 6N (NASA LP DAAC, 2015; Table S3, data downloaded from https://lpdaac.usgs.gov). Since ground control points were not available, more than 200 tie points for each scene, covering different altitudes and surfaces including ice and snow, were automatically collected and then manually examined (removing those influenced by clouds or water) for all stereo-pairs. The maximum Y parallax errors of the tie points were constrained to less than one pixel (±15 m). The DEMs were generated with 30 m resolution. Artifacts, which mainly resulted from clouds and other noises, were removed using a median filter. All extracted ASTER DEMs cover the glacierized area and surrounding terrain within ~10 km from the ice margin.

The resulting DEMs may contain planimetric and altimetric biases (Moore and others, 2002; Molnia, 2007; Berthier and others, 2010). The DEM biases caused by misregistration between DEMs were corrected by the co-registration method suggested by Nuth and Kääb (2011), which depends on the elevation differences, slope and aspect over stable terrain. The IFSAR DEM was used as master DEM after resampling to 30 m spatial resolution using pixel assembly, and all DEMs (ASTER DEMs and IFSAR DEM) were referenced to the same datum and projection. Only the DEM differences of pixels that do not contain glaciers, water bodies and vegetation (determined by the land cover map of Alaska, USGS (2011)) were used to derive the adjustment coefficients. Then the IQR (see section 3.2.1) was adopted to remove outliers which were typically caused by clouds, data gaps and DEM edges. All iterations of the co-registration adjustment were stopped when the improvement in Std dev. of elevation difference on stable terrain was <2%. Then the along/cross track biases of all ASTER DEMs related to satellite acquisition geometry were corrected using higher order polynomial fittings (5^{th} to 8^{th} order; Nuth and Kääb, 2011).

Figure 2 illustrates the co-registration of the ASTER DEM (image AST-4, Table S3) to IFSAR DEM. Table 1 and Figure 3

https://doi.org/10.1017/jog.2020.32 Published online by Cambridge University Press

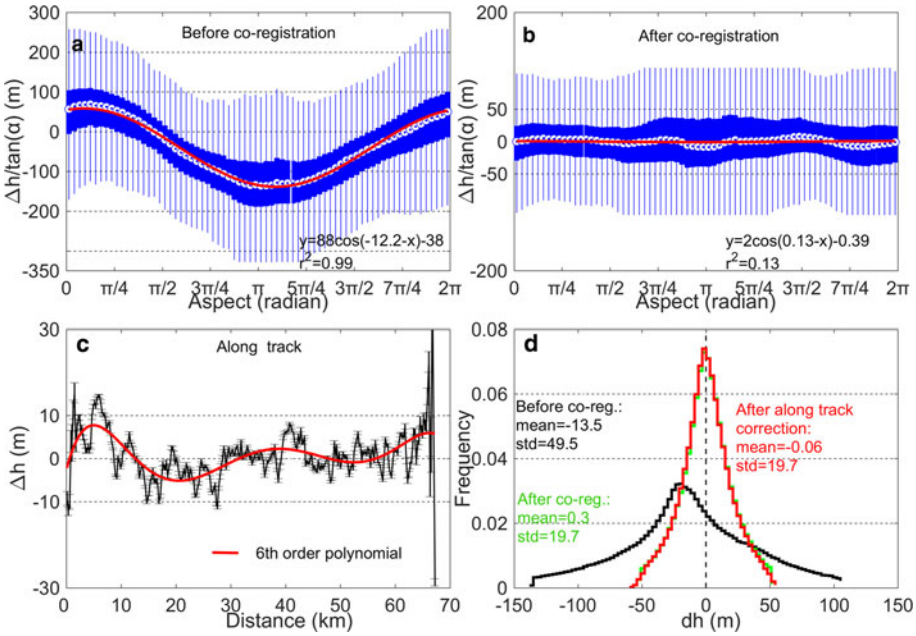

Fig. 2. Results of the co-registration of the ASTER DEM (AST-4) to the IFSAR DEM. (a, b) Elevation differences normalized by the slope tangent vs aspect (a) before co-registration and (b) after co-registration, including error bars (blue) and cosine-fit (red line). The fitted equation and coefficient of determination r^2 are given in the lower right corner. (c) Residual elevation difference with error bars in the along-track direction. (d) Normal probability density curve of elevation differences. The bin size is 0.0175 (5°) for panels (a) and (b), and 500 and 3 m for panels (c) and (d), respectively.

Table 1. Statistics of elevation differences between ASTER DEMs (AST-1, AST-2a, b, AST-4) and IFSAR DEM over stable terrain after co-registration and after additional along/cross track correction. The grid resolution is 30 m. *N* is the number of pixels, $\overline{\Delta h}$ is the mean elevation difference (*m*) and σ_{non} is the Std dev. of elevation difference (*m*), d*x*, d*y*, d*z* are the three components of the full co-registration adjustment vector (in meters) between the ASTER DEMs and IFSAR DEM.

		Original		After co-registration				After along/cross track correction		
Image	*N*	$\overline{\Delta h}$ *m*	σ_{non} *m*	d*x* *M*	d*y* *m*	d*z* *m*	σ_{non} *m*	Type	$\overline{\Delta h}$ *m*	σ_{non} *m*
AST-1	272 688	−30.5	54.3	22.5	−18.2	−39.5	48.9	Along/cross	−0.11	46.7
AST-2a	568 285	−82.5	59.1	−46.3	−37.1	−87.8	46.1	Along	0.42	43.5
AST-2b	505 416	1.96	37.2	26.2	62.0	−0.96	21.6	Along	0.15	21.3
AST-4	761 879	−13.5	49.5	34.1	129	−22.2	19.7	Along	−0.06	19.7

show the co-registration vectors and correction results of each DEM pair.

3.2.3 Elevation changes

The co-registered ASTER DEMs were subtracted from the IFSAR DEM to calculate elevation difference (*dh*) over the glacierized areas of the four subregions I–IV (Fig. 1). After scrutinizing the elevation difference maps and difference histograms, we regard pixels with $dh\ dt^{-1}$ values >5 m a^{-1}, < −15 m a^{-1} for elevations below 1000 m a.s.l. (−10 m a^{-1} for subregion I) and < −5 m a^{-1} for elevations higher or equal 1000 m a.s.l. as outliers. This procedure proved to be the most suitable approach in this region compared to other methods, such as empirical value (Berthier and others, 2010; Bolch and others, 2011), IQR (O'Neel and others, 2014; Fischer and others, 2015; Kienholz and others, 2015; Pieczonka and Bolch, 2015).

Data gaps were filled with the mean value of the elevation change in each 50 m elevation band (Fig. 4), which has been proven as an effective method to interpolate voids in DEM difference maps and can tolerate a rather high percentage of data voids, up to ~60% (McNabb and others, 2019).

3.2.4 Volume and mass change

Glacier volume changes for each subregion and period were computed by multiplying the mean surface elevation changes by the glacier area in 2005 (Tables 2 and 3). A volume to mass conversion factor of 850 ± 60 kg m^{-3} (Huss, 2013) was used.

3.2.5 Correcting for difference in DEM acquisition dates

To account for the temporal difference in DEM acquisition (9 August and 14 August 2005 for ASTER and between 29 August and 12 September 2014 for IFSAR), we approximated the mass change that occurred between 11 August and 6 September 2005, and adjusted the area-averaged specific mass change rates obtained above accordingly for each subregion. Following Van Beusekom and others (2010), we used a simple degree-day mass balance model forced by daily temperature and precipitation data from the Wolverine weather station (990 m a.s.l.) to compute idealized mass-balance profiles for the elevation range of the glacier-covered area (0–2000 m a.s.l.). Since the model is not well-constrained, we applied Monte Carlo methods to randomly vary model parameters within reasonable limits and generated 50 profiles. Model parameters and applied ranges are given in Supplementary Table S5. The mass-balance profiles, which provide a mass-change value for each elevation, were assumed constant across the corresponding glacier regions, and used to compute a mass change for each glacierized gridcell. Area-averaged mass changes were computed for each subregion. Over the 27 days, the total mass change in the period 11 August to 6 September 2005 ranged from −0.86 ± 0.17 m w.e. (subregion III) to −0.73 ± 0.17 m w.e. (subregion II) with a region-wide average of −0.78 ± 0.10 m w.e..

3.3 Uncertainty estimation

3.3.1 Glacier outlines

Glacier area errors normally include technical errors (misregistration), interpretation errors and methodological constraints (Raup

https://doi.org/10.1017/jog.2020.32 Published online by Cambridge University Press

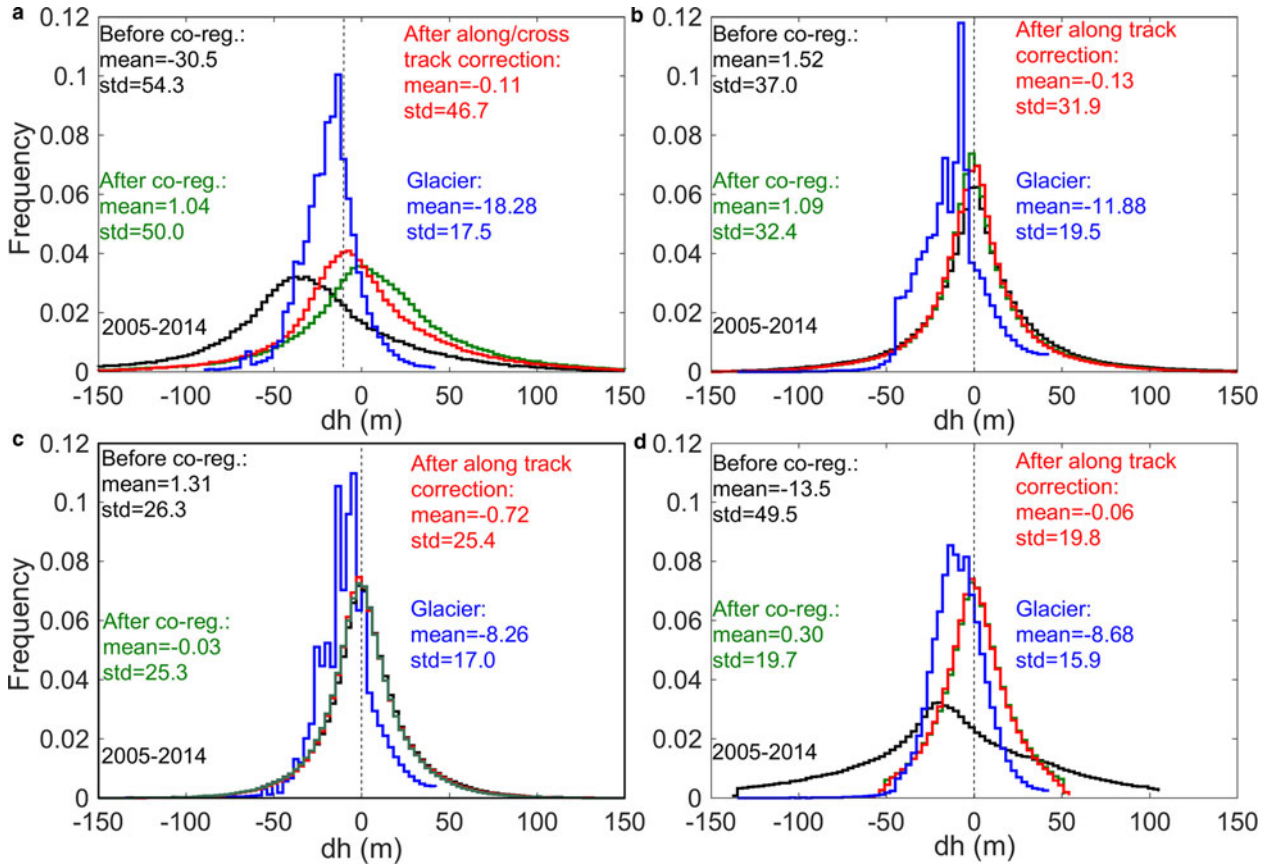

Fig. 3. Frequency distribution of elevation changes d*h* over stable terrain and the glacier area during the study period. Bin size is 3 m. Mean and Std dev. is given for various stages of co-registration (Fig. 2). Panels a, b, c and d refer to the subregions I, II, III and IV (Fig. 1), respectively.

and others, 2007; Paul and Andreassen, 2009). In this study, the band ratio method was used to derive almost all glacier outlines from Landsat data and no distinct horizontal shift between images was found when visually checking over stable landforms (e.g. mountain ridges, peaks or lateral moraines), so the technical error was considered negligible and ignored (Bolch and others, 2010; Guo and others, 2013). Interpretation errors are mostly associated with the definition of a glacier, while methodological errors largely depend on the resolution of the source imagery, and the experience of compilers. Following Guo and others (2015), we incorporated all error sources into one term, assuming ±10 and ±30 m accuracies for clean-ice and debris-covered glacier outline delineation respectively, and ±5 m for ice divides.

The buffer method was selected to calculate the uncertainty of glacier area generated from Landsat images, which included both the length of glacier outlines and positional accuracies (e.g. Rivera and others, 2005; Granshaw and Fountain, 2006; Kienholz and others, 2015; Tielidze and Wheate, 2018). The area error of each individual glacier E_a, was defined as,

$$E_a = \sum_{i=1}^{n} L_i E_{pi} \tag{1}$$

where, i is the type of glacier outlines (clean-ice, debris-covered, ice divides, $n = 3$) and L_i is the length of glacier outline and E_{Pi} is the position error. The errors of the position of the ice divides were omitted for considering the whole glacier area of each subregion, and the errors of boundary between clean and debris-covered ice were omitted in the single and regional glacier area error estimation.

The uncertainty of area change $E_{\Delta A}$ over a period t_1–t_2, was calculated by

$$E_{\Delta A} = \sqrt{E_{A1}^2 + E_{A2}^2} \tag{2}$$

where E_{A1} and E_{A2} are the errors of the glacier area in t_1 and t_2, respectively.

3.3.2 Elevation change

Following Zemp and others (2013) and Huber and others (2020), the uncertainty of area-averaged elevation change (σ) was estimated from three components: the uncertainty related to spatial autocorrelation in elevation differences ($\sigma_{autocorr}$), the uncertainty related to the residual elevation errors after co-registration (σ_{coreg}) and the uncertainty due to data voids (σ_{void}), although this approach may underestimate the total error (Berthier and others, 2012, 2016).

$$\sigma = \sqrt{\sigma_{autocorr}^2 + \sigma_{coreg}^2 + \sigma_{void}^2} \tag{3}$$

The Std dev. of the elevation differences between the ASTER DEMs and IFSAR DEM over nonglacierized pixels (stable terrain; σ_{non}) can be used as a first estimate of the $\sigma_{autocorr}$, if the spatial correlation of the elevation differences is accounted for (Rolstad and others, 2009). Following Gardelle and others (2013), we calculated the standard error (SE) of the mean elevation change:

$$\mathrm{SE} = \frac{\sigma_{non}}{\sqrt{N_{eff}}} \tag{4}$$

https://doi.org/10.1017/jog.2020.32 Published online by Cambridge University Press

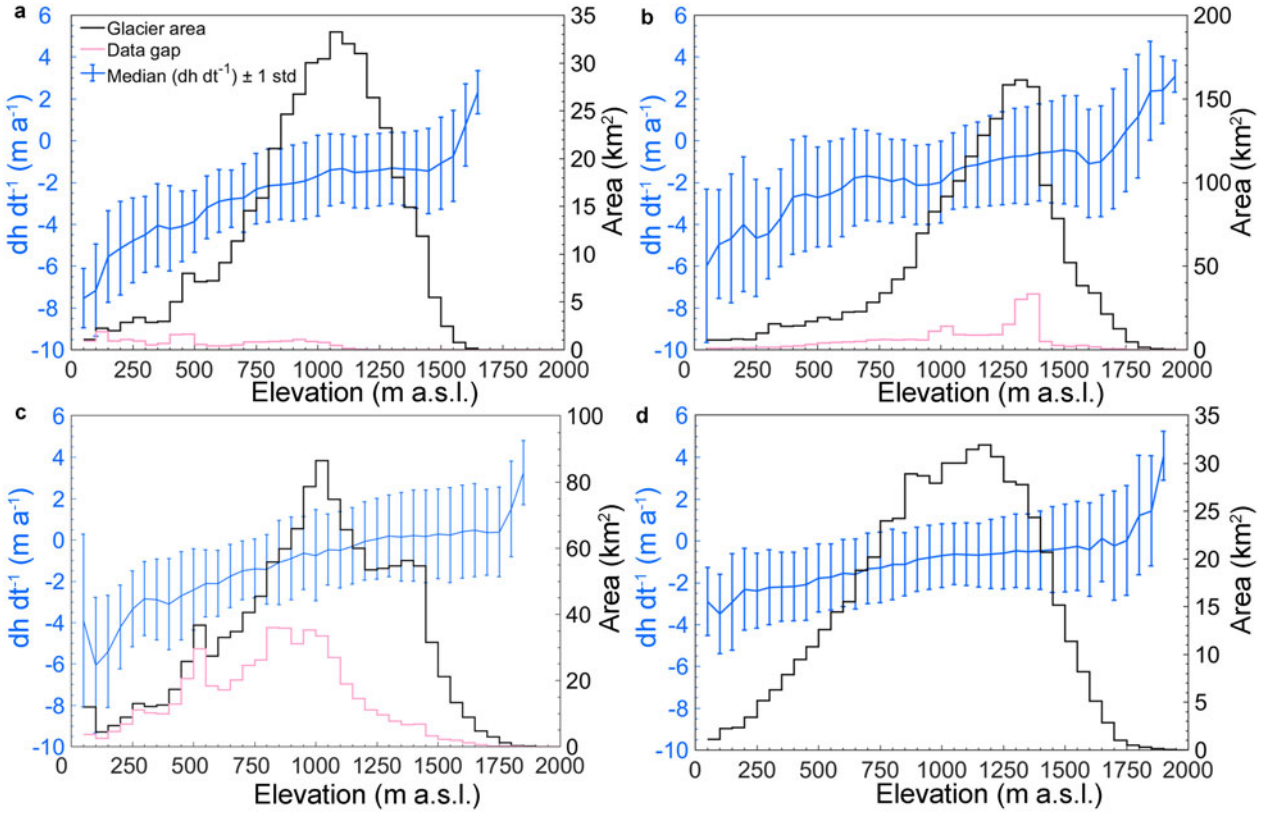

Fig. 4. Elevation change rates (blue) for all glacierized cells of ASTER DEMs for which data were available (median ± 1 Std dev.) and area-altitude distribution (50 m bin size) of total glacier area (black), and the area with data gaps (pink). The panels a, b, c and d represent the four subregions I, II, III and IV, respectively (Fig. 1).

Table 2. Glacier area in 1986, 1995, 2005, 2016 for four regions (Fig. 1) and the area change 1986–2016

	Area (km^2)				Area change (1986–2016)	
Region	1986	1995	2005	2016	km^2	%
I	466 ± 11	457 ± 11	427 ± 11	408 ± 12	−58 ± 16	−12 ± 3
II	1976 ± 32	1931 ± 30	1827 ± 33	1781 ± 35	−195 ± 47	−10 ± 2
III	1315 ± 24	1276 ± 22	1229 ± 23	1151 ± 23	−164 ± 33	−12 ± 3
IV	643 ± 20	615 ± 18	559 ± 17	517 ± 17	−126 ± 26	−20 ± 4
Total	4400 ± 87	4279 ± 81	4087 ± 84	3857 ± 87	−543 ± 123	−12 ± 3

where N_{eff} is the effective number of the pixels after de-correlation defined by,

$$N_{eff} = \frac{N_{tot} \cdot R}{2d} \quad (5)$$

where N_{tot} is the total number of pixels on the nonglacierized area (stable terrain); R is the pixel size (30 m), d is the de-correlation distance assumed to be 600 m as suggested by Bolch and others (2011) and also used in previous geodetic mass-balance studies (Brun and others, 2017; Menounos and others, 2019; Pelto and others, 2019). $\sigma_{autocorr}$ was then calculated using $\overline{SE}$ and the mean elevation differences of the nonglacier region ($\overline{\Delta h}$):

$$\sigma_{autocorr} = \sqrt{\mathrm{SE}^2 + \overline{\Delta h}^2} \quad (6)$$

σ_{coreg} was calculated using the triangulation method by Nuth and Kääb (2011). Based on three elevation data sets (ASTER DEM, IFSAR DEM and ICESat), we did co-registration by the correction vectors between each of them and then used the residual between the triangulation of vertical vectors to estimate σ_{coreg} (Table S6).

The DEM difference maps include data voids encompassing 7, 19, 41 and 1% of the four subregions I, II, III and IV, respectively. Based on findings by McNabb and others (2019), who derived differences to true elevation changes as a function of void percentage, we used the constant values of 0.05 and 0.10 m a^{-1} to estimate σ_{void} for subregions II and III, respectively, and assumed zero σ_{void} for subregions I and IV due to nearly complete coverage.

3.3.3 Errors in volume and specific mass changes

Following standard error propagation, we finally obtained the error of the volume change E_{Vol} and specific mass balance E_{Mass} (m w.e. a^{-1}), assuming that error terms are independent of each other by

$$E_{Vol} = \sqrt{(dh \cdot E_A)^2 + (A \cdot \sigma)^2} \quad (7)$$

where A is the glacier area in 2005, E_A is the corresponding error.

$$E_{Mass} = \sqrt{(dh \cdot E_\rho)^2 + (\sigma \cdot \rho)^2} \quad (8)$$

where ρ is the assumed volume to mass conversion factor (850 kg m^{-3}), E_ρ is the corresponding error (±60 kg m^{-3}); dh is area-averaged surface elevation change, while σ is the corresponding elevation change error (Eqn (3)). The mean annual uncertainty is then given by dividing E_{Mass} by the number of years.

https://doi.org/10.1017/jog.2020.32 Published online by Cambridge University Press

Table 3. Glacier-wide mean rates of elevation change ($dh\,dt^{-1}$), volume change ($dV\,dt^{-1}$), specific mass change ($dM\,dt^{-1}$) in each subregion (Fig. 1) for 2005–2014. Area refers to the glacier area in 2005. The region-wide average is the area-weighted average of the four subregions

Region	Period	Area km^2	$dh\,dt^{-1}$[a] m a^{-1}	$dV\,dt^{-1}$[a] km^3 a^{-1}	$dM\,dt^{-1}$[a] m w.e. a^{-1}	$dM\,dt^{-1}$[b] m w.e. a^{-1}
I	2005–2014	427 ± 11	−2.03 ± 0.29	−0.87 ± 0.13	−1.73 ± 0.27	−1.63 ± 0.28
II	2005–2014	1827 ± 33	−1.32 ± 0.25	−2.41 ± 0.46	−1.12 ± 0.23	−1.04 ± 0.23
III	2005–2014	1229 ± 23	−0.92 ± 0.23	−1.13 ± 0.29	−0.78 ± 0.21	−0.69 ± 0.21
IV	2005–2014	559 ± 17	−0.96 ± 0.14	−0.54 ± 0.08	−0.82 ± 0.13	−0.73 ± 0.13
I–IV	2005–2014	4087 ± 84	−1.21 ± 0.14	−4.95 ± 0.57	−1.03 ± 0.12	−0.94 ± 0.12

[a]Based on original acquisition dates of IFSAR (29 August–12 September 2014) and ASTER DEM (09 August–14 August 2005).
[b]Includes correction for seasonal difference in acquisition data, so that the ASTER data refers to 6 September (Section 3.2.4).

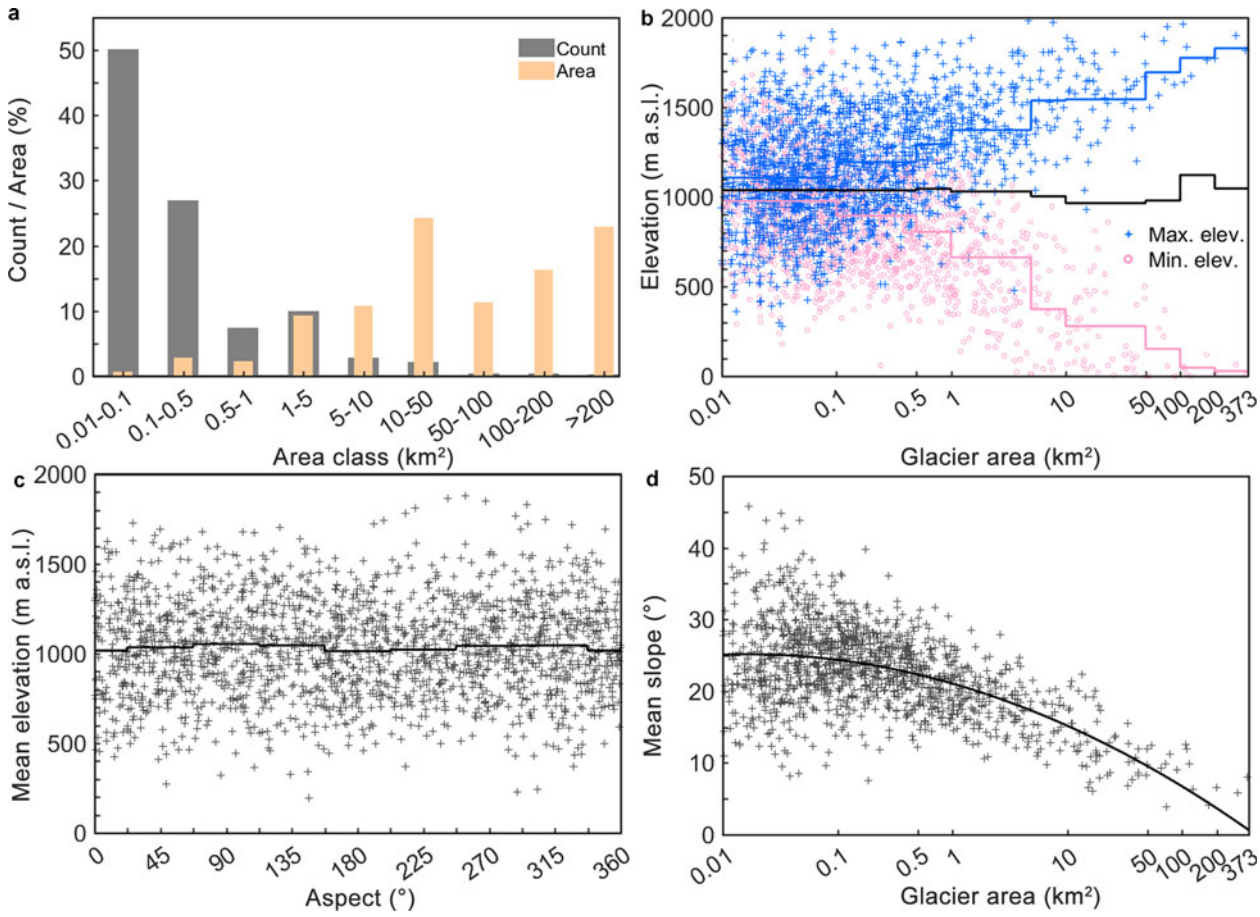

Fig. 5. Characteristics of glacier distribution of Kenai Peninsula in 2016. (a) Distribution of glaciers in different area classes; (b) scatterplot of glacier size vs maximum and minimum elevation (Max. elev., Min. elev.). The solid lines (blue and pink) give mean values for distinct size classes while the dark line shows the median elevation per area class for the same area classes as shown in (a); (c) Mean elevation vs aspect per glacier; the solid line refers to the mean per cardinal sector; (d) Mean slope vs glacier size per glacier. The solid line shows the trend (2nd polynomial fit). *X*-Axis in (b) and (d) is logarithmically transformed.

4. Results and discussion

4.1 Glacier inventory in 2016

In the 2016 Landsat inventory (L2016), the 1357 glaciers larger than 0.01 km^2 cover an area of 3857 ± 87 with 35 ± 12 km^2 (~1%) of the surface debris covered. Half of the glaciers are smaller than 0.1 km^2, but they contribute only to <1% to the total area. Only 76 glaciers (~6%) are larger than 5 km^2, however, they make up about 85% of the total area (Fig. 5a).

Figure 5b indicates that the glaciers' minimum elevation decreases while their maximum elevation increases as the glacier size increase, indicating that glaciers reaching sea-level require a large elevation range, similar to the findings on southern Baffin Island (Paul and Svoboda, 2009). The median elevation of all glaciers fluctuates slightly around ~1100 m a.s.l., regardless area class which may indicate that the equilibrium line of the Kenai Peninsula glaciers is at a similar elevation. There is no correlation between mean glacier elevation and aspect (Fig. 5c). As expected, the mean glacier slope decreases with glacier size, but the scatter is large for smaller glaciers (Fig. 5d) due to local topography (Haeberli and Hoelzle, 1995; Paul and others, 2011).

Figure 6 illustrates the area distribution per elevation, slope and aspect class for each subregion as well as the entire region. Nearly all ice-covered area (>99%) is situated between 150 m and 1750 m a.s.l. (Fig. 6a). The area-elevation distribution of subregion II peaks at a higher elevation than the remaining regions. As shown in Figure 6b, glacier area with slopes <30° occupies 90% of the total area. Figure 6c indicates that there is a tendency for glacierized pixels in all subregions to face towards the northwest or east.

https://doi.org/10.1017/jog.2020.32 Published online by Cambridge University Press

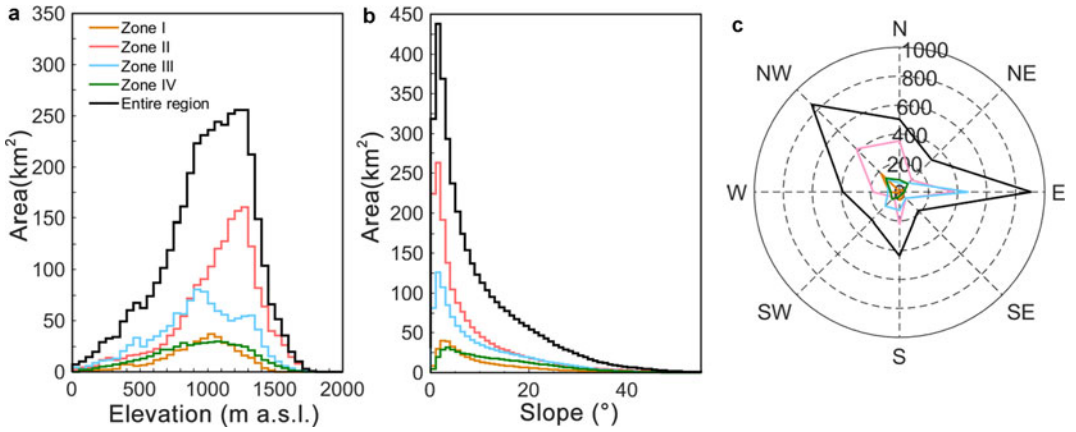

Fig. 6. Area distribution of topography variables for glacierized area in each subregion (I, II, III and IV) and the entire region in 2016 including (a) hypsography with bin size 50 m, and (b) slope with bin size of 1°; (c) aspect, in which numbers represent the glacier area with unit km^2 in 22.5° aspect bins.

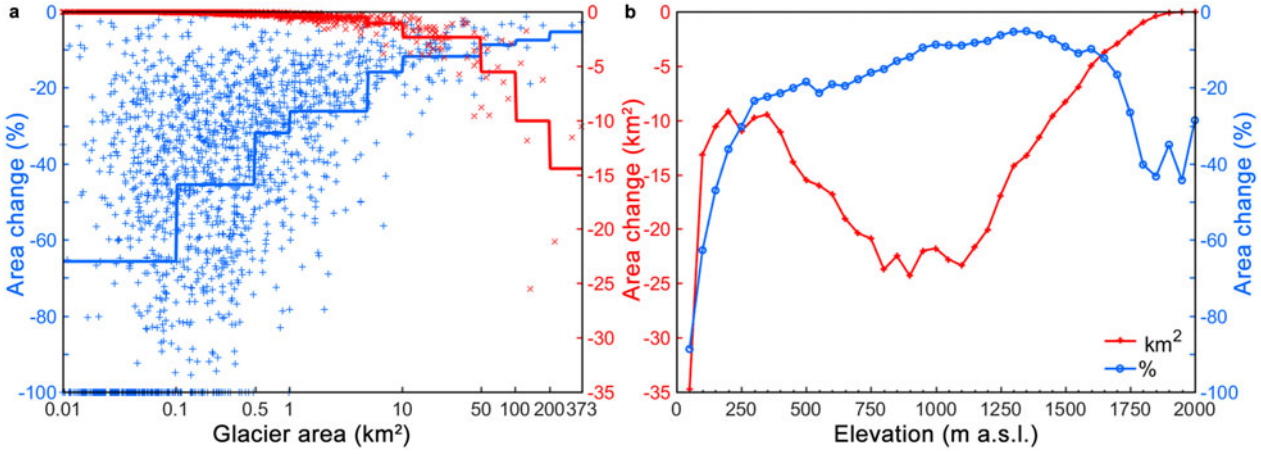

Fig. 7. (a) Relative (blue) and absolute (red) glacier area change between 1986 and 2016 (a) for each glacier (n = 1660) as a function of glacier area, and (b) as a function of elevation (based on all glacier pixels falling within sequential 50 m bins). Solid lines in (a) show the mean values per area class.

4.2 Area change

Total glacier area has shrunk by 543 ± 123 km^2 (12 ± 3%) between 1986 and 2016. Glaciers in different regions retreated at different speeds (Table 2) and the highest area loss rate occurred in subregion IV (total area loss of 20 ± 4%).

Larger glaciers tend to have smaller relative area losses than smaller glaciers, but the scatter especially for the smaller glaciers is large (Figs 7a, 8b), consistent with previous studies (Maisch and others, 1999; Serandrei Barbero and others, 1999; Kääb and others, 2002; Paul, 2002; DeBeer and Sharp, 2009; Bolch and others, 2010). The average area loss for glaciers <0.5 km^2 is nearly 56%, ranging from 0 to 100%, while it is 8% for glaciers larger than 10 km^2. Approximately 270 glaciers (all <0.5 km^2) disappeared during 1986–2016. Larger retreat rates of smaller glaciers can be attributed to a stronger impact of local topographic characteristics on the processes controlling the glacier mass balance (Florentine and others, 2018). For example, a moderate rise in the equilibrium line may turn the entire glacier to ablation zone (Kaser and Osmaston, 2002; Racoviteanu and others, 2008*b*). A given specific mass change may also result in larger relative area changes for smaller and thinner glaciers than larger glacier with steeper flanks (Kääb and others, 2002). Generally, the area loss rate decreases with increasing elevation (Fig. 7b) except for elevations above 1700 m a.s.l. where the sample size is very small and errors most likely larger due to steep terrain, cast shadows and seasonal snow.

For glaciers smaller than 0.1 km^2 (nearly 50% of the total number of glaciers) with a more notable reduction in area than others, the area loss during 2005–2016 is markedly lower than during the earlier periods of 1986–1995 and 1995–2005 (Fig. 8b). One possible explanation is that small glaciers may retreat into more sheltered locations that facilitate their preservation (DeBeer and Sharp, 2009).

We investigated the role of the slope and aspect in spatial variations in area change. Results show that slope played an important role in relative glacier area reduction. Glaciers located on steeper terrains experienced larger relative area loss than less steep glaciers (Fig. 8c) consistent with previous studies (Salerno and others, 2008; Racoviteanu and others, 2015; Tielidze and Wheate, 2018). Southeast-south-southwest facing glaciers experienced generally more pronounced shrinkage than northwest-north-northeast facing glaciers. This is similar to the pattern found in the Himalaya by Ahmad and Rais (1999), which was attributed to more solar radiation on the south-facing than north-facing slopes.

4.3 Glacier elevation and mass changes

Figure 9 shows the spatial distribution of surface elevation changes for the four subregions during 2005–2014. All regions experienced most pronounced thinning in the lower parts

https://doi.org/10.1017/jog.2020.32 Published online by Cambridge University Press

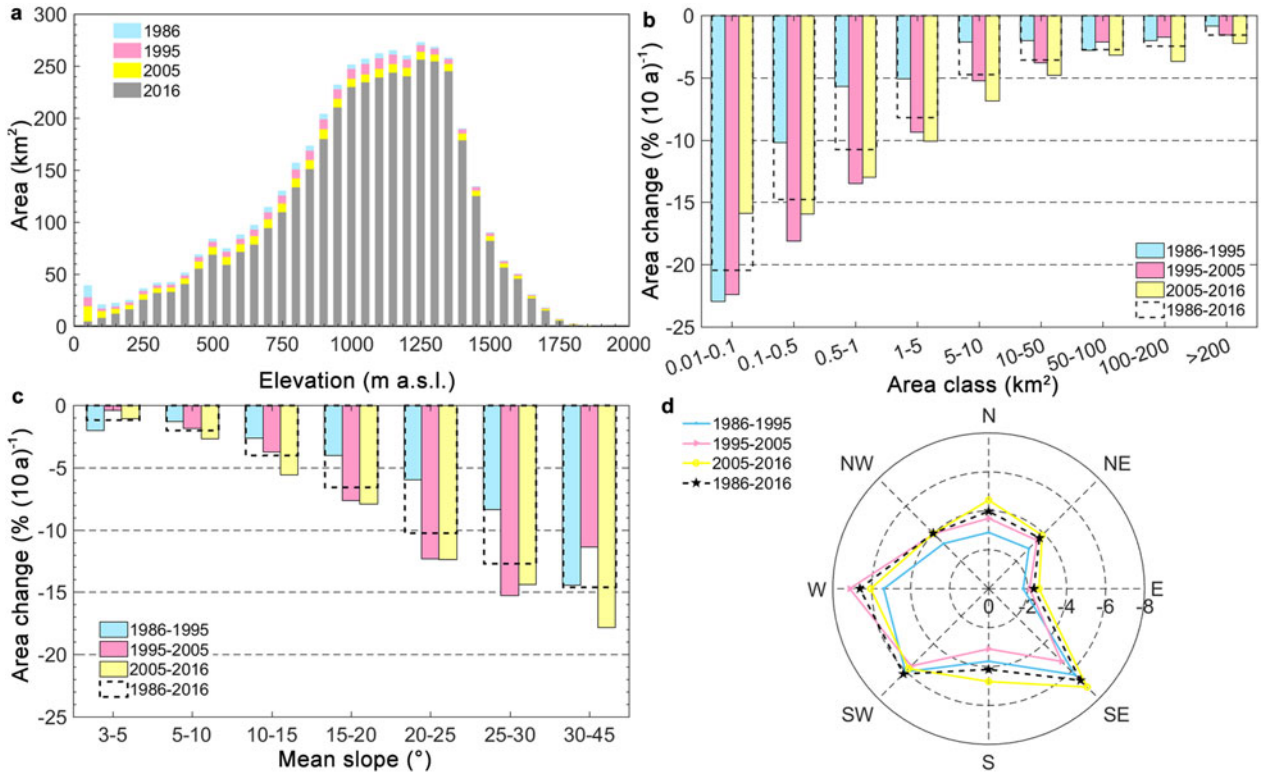

Fig. 8. (a) Glacier area-elevation distribution for four different years, and (b–d) glacier area-change rates for different periods between 1986 and 2016 vs (b) area size class, (c) mean slope and (d) aspect. The bin size in panel a is 50 m. Numbers in panel d refer to area change rates in % $(10\,a)^{-1}$.

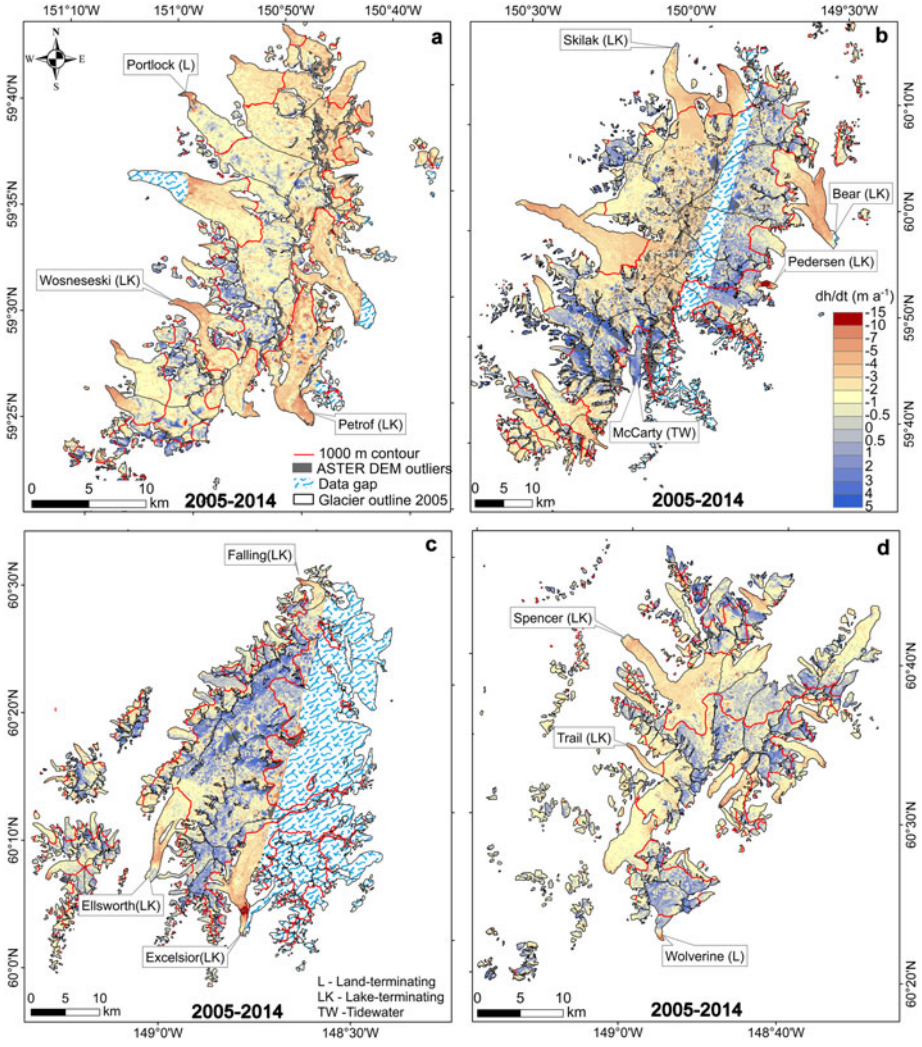

Fig. 9. Spatially distributed surface elevation changes rates for the period 2005–2014. Dark gray areas represent the cloud error mask of the ASTER DEM, while white area with blue dashes mark the areas with no data. The red line is the 1000 m contour line. The panels a, b, c and d represent the four sub-regions I, II, III and IV, respectively (Fig. 1).

https://doi.org/10.1017/jog.2020.32 Published online by Cambridge University Press

Table 4. Area (% of total), mean elevation and specific mass balance ($dM\,dt^{-1}$ in m w.e. a^{-1}) during the period 2005–2014 for three glacier types (land-terminating, lake-terminating and tidewater glaciers) in each subregion (Fig. 1). Area refer to the inventory from 2005 and elevations to the IFSAR DEM in 2014

	Area per glacier type, Mean elevation			$dM\,dt^{-1}$			Mean elevation (range)
	%, m a.s.l.			m w.e. a^{-1}			
Subregion	Land-term.	Lake-term.	Tidewater	Land-term.	Lake-term.	Tidewater	m a.s.l.
I	57, 986	43, 875	0, –	−1.49 ± 0.27	−1.90 ± 0.24	–	939 (15–1655)
II	57,1094	22,1060	21,1147	−1.16 ± 0.23	−1.44 ± 0.24	−0.42 ± 0.22	1098 (0–1967)
III	39, 931	22, 937	39, 948	−0.73 ± 0.20	−0.97 ± 0.21	−0.50 ± 0.20	939 (0–1888)
IV	68, 966	21, 915	11, 948	−0.72 ± 0.13	−1.22 ± 0.15	−0.26 ± 0.12	954 (0–1980)
I–IV	53,1023	24, 975	23,1033	−1.02 ± 0.13	−1.37 ± 0.13	−0.45 ± 0.14	1014 (0–1980)

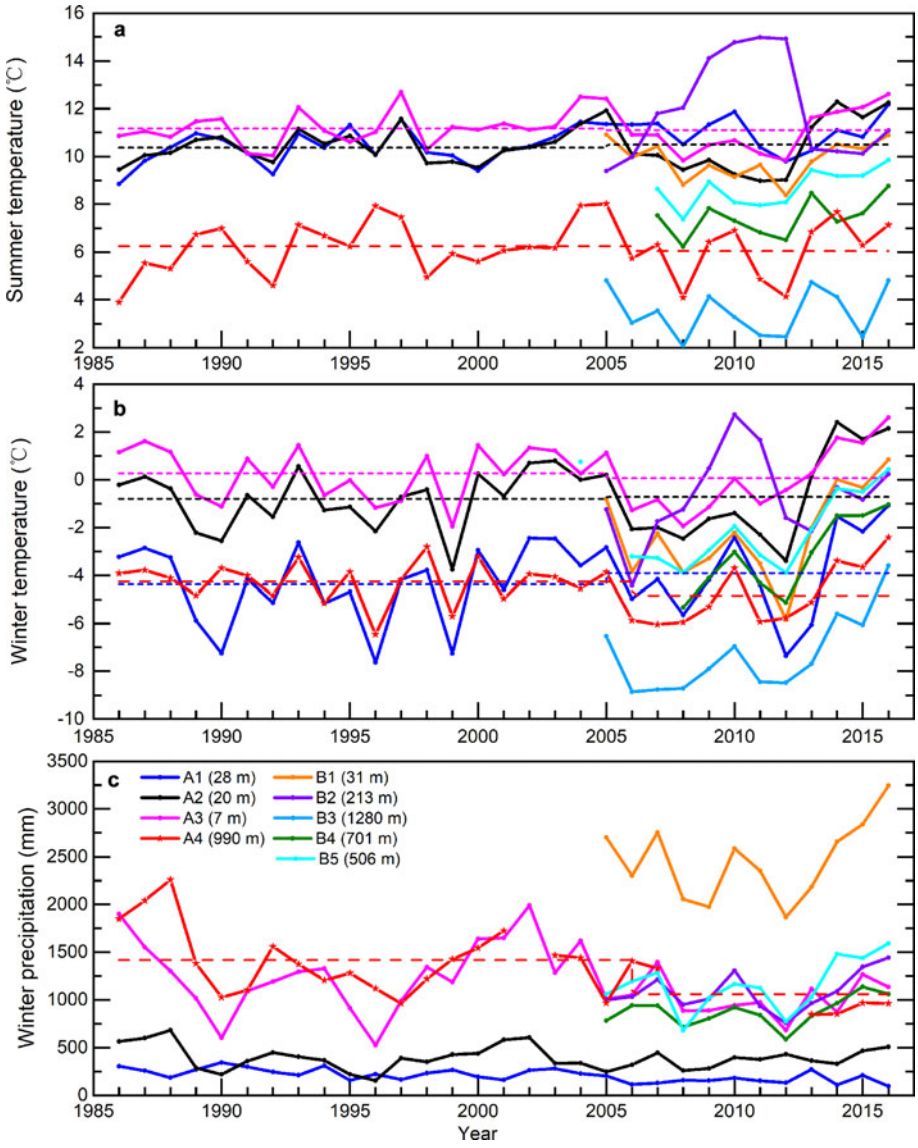

Fig. 10. Time series of (a) summer (May to September) temperature, (b) winter (October to April) temperature and (c) winter (October to April) precipitation for eight weather stations in the Kenai Peninsula (Fig. 1) in the period 1986–2016. Dotted lines are the mean values before and after 2005 when an abrupt change was detected with statistical significance $\alpha = 0.05$ (Fig. 11). Numbers in parentheses indicate the elevation of each weather station (m a.s.l.). Precipitation data are not available for B3. Data from NOAA, except A4 (Wolverine weather station), from the USGS.

especially below 1000 m a.s.l., and less pronounced thickening or thinning in the glaciers' upper reaches.

In subregion I (Grewing-Yalik glacier complex), most thickening occurred above 1000 m a.s.l., but the lower tongue of Portlock Glacier and some smaller glaciers in the southeast show some thickening at lower elevations (Fig. 9a). In subregion II (Harding Icefield), especially the upper reaches of some glaciers in the southwest and southeast experienced thickening. It remains unclear whether this thickening is caused by net snow accumulation, changes in ice dynamics or by errors due to the noise of ASTER DEM (Fig. 9b). Large parts of McCarty Glacier (<1000 m a.s.l.) show a positive surface elevation change, similar to results found by Aðalgeirsdóttir and others (1998) for the period 1950s–1990s.

The two lake-terminating glaciers (Falling and Excelsior glacier), experienced extreme thinning close to their termini (nearly 15 m a^{-1}). The lower tongue of Ellsworth Glacier shows glacier thickening during the studied period (Fig. 9c). However, based on recent satellite imagery, no evidence of a surge could be detected that could explain the local thickening. More studies, such as the surface velocity and its recent dynamics, or the distribution of its thickness, are needed to reveal its causes. Errors in the DEMs may also explain this anomaly.

https://doi.org/10.1017/jog.2020.32 Published online by Cambridge University Press

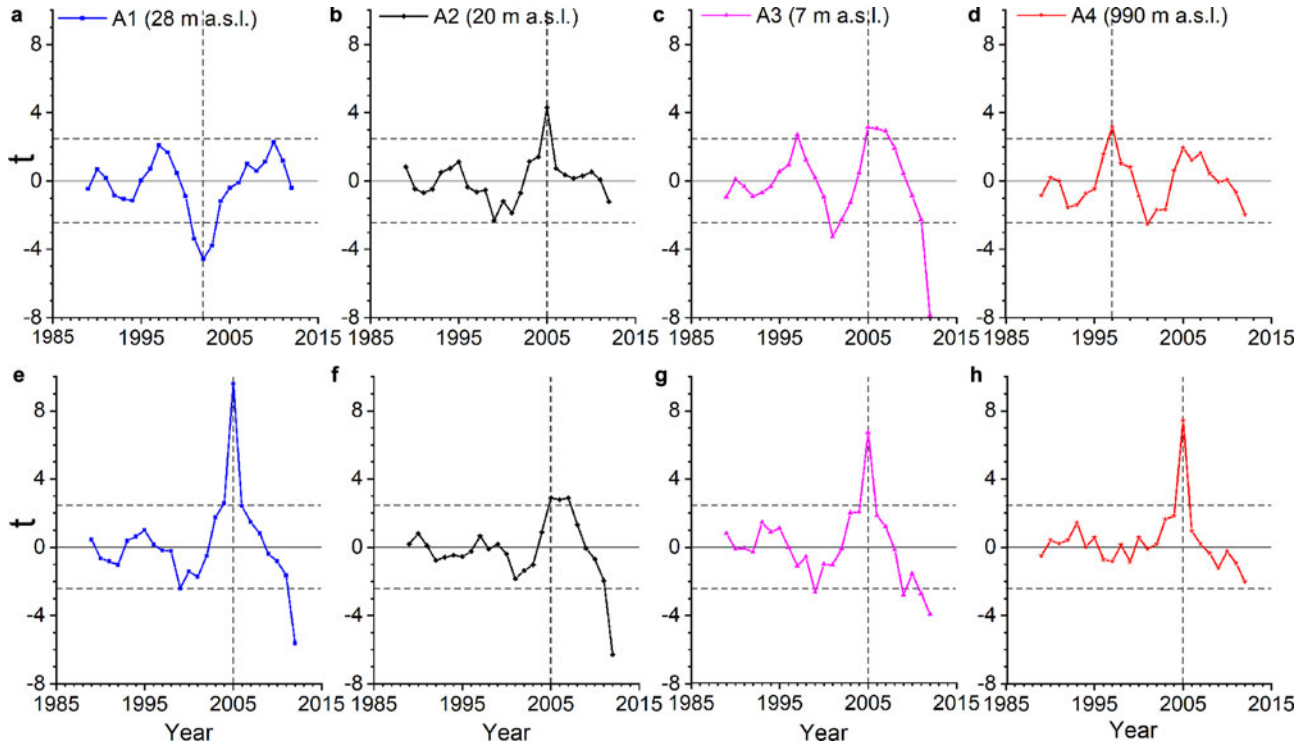

Fig. 11. The moving *t*-test curve of the air temperatures of four weather stations (A1, A2, A3 and A4) on the Kenai Peninsula. Dashed horizontal lines indicate the 95% confidence level ($\alpha = 0.05$). Results indicate an abrupt change in 2005 (or 2002 in panel a, 1997 in b). Panels a–d refer to summer temperatures, while panels e–h refer to winter temperatures.

The regional elevation and mass changes during 2005–2014 for the four subregions are given in Table 3. Results emphasize the need to correct for differences in acquisition dates of any two DEMs to be differenced in regions with considerable mass change over short periods. Without accounting for the 27-days elevation difference between the ASTER DEMs and IFSAR DEM acquisition date, the area-average region-wide mass-balance rate would have been underestimated by 0.09 m w.e. a^{-1} (~10%).

On average the glaciers on the Kenai Peninsula experienced specific mass changes of -0.94 ± 0.12 m w.e. a^{-1}. Mass-balance rates were most negative for lake-terminating glaciers (-1.37 ± 0.13 m w.e. a^{-1}, ~980 km^2), followed by land-terminating glaciers (-1.02 ± 0.13 m w.e. a^{-1}, ~2166 km^2) and tidewater glaciers (-0.45 ± 0.14 m w.e. a^{-1}, ~941 km^2). This pattern cannot be explained with differences in mean elevation (Table 4). Many lake- or marine-terminating glaciers experienced pronounced thinning especially on their tongues (Wosneseski, Petrof, Skilak, Bear, Pedersen, Falling, Excelsior, Spencer and Trail glaciers; Fig. 9), but not all (for example McCarty glacier). This trend is consistent with airborne laser altimetry derived results across Alaska (Larsen and others, 2015), which indicated more rapid thinning of many lake-terminating glaciers near their termini compared to land-terminating glaciers.

Mean specific mass change rates varied considerably among the four subregions (Table 3). Subregion I (Grewing-Yalik glacier complex) experienced the most negative mean mass change (-1.63 ± 0.28 m w.e. a^{-1}), and subregion III (Sargent Icefield) the least negative rate (-0.69 ± 0.21 m w.e. a^{-1}). These differences are consistent with the relative distribution of glacier types. Subregion I has roughly twice as much lake-terminating glacier area (in %) than the other subregions while tidewater glaciers are lacking. In contrast subregion III has a considerably higher percentage of tidewater glacier area compared to the other regions (Fig. 1, Table 4).

Wolverine glacier (~17 km^2, Fig. S3), located in subregion IV and part of the USGS benchmark glacier monitoring project, had an average glacier-wide mass-balance rate of -0.55 m w.e. a^{-1} during the period 2005–2014 (O'Neel and others, 2019), is similar to the averaged mass-balance rate of subregion IV (-0.73 ± 0.13 m w.e. a^{-1}). However, we find a less negative mass-balance rate for Wolverine glacier for the same period (-0.20 ± 0.13 m w.e. a^{-1}) and attribute this discrepancy to artifacts in the DEMs which are introduced by the steep local topography (Koblet and others, 2010; Le Bris and Paul, 2015).

4.4 Comparison with other studies

Our new Landsat derived glacier inventory of the Kenai Peninsula for 2005 includes 1421 glaciers covering an area of 4087 ± 84 km^2, which agrees well with RGI 6.0 (1457 glaciers, ~4175 km^2, Kienholz and others, 2015) compiled in 2005–2007. Hall and others (2005) found an area reduction of 3.6% (~78 km^2) for the Harding Icefield and Grewingk-Yalik Glacier Complex (excluding the glaciers in the surroundings that are not connected to these ice fields) over the time interval 1986–2002. Their results are similar to our results for 1986–2005 for the same ice masses (area loss of 91 ± 22 km^2, 4.2%). O'Neel and others (2019) found that the Wolverine glacier experienced a 1.5 km^2 area reduction between 1969 and 2018, which is similar to the area loss of 1.4 km^2 found in this study for the period 1986–2016.

Aðalgeirsdóttir and others (1998) calculated a surface thinning rate for the Harding Icefield (subregion II) of -0.49 ± 0.12 m a^{-1} for the period 1950s–1996, which is close to the rate of -0.47 ± 0.01 m a^{-1} found by VanLooy and others (2006) for roughly the same period (1950 to mid-1990s). The latter study found an accelerated rate of surface elevation change (-0.72 ± 0.13 m a^{-1}) in the period mid-1990s to 1999. For the glaciers in subregions I and II combined, they report a surface elevation change rate of -0.61 ± 0.12 m a^{-1} for the entire period 1950–1999. Correspondingly, we find accelerated elevation change rates of -1.97 ± 0.29 and -1.26 ± 0.25 m a^{-1} for subregions I and II (the area-average

https://doi.org/10.1017/jog.2020.32 Published online by Cambridge University Press

value is -1.39 ± 0.21 m a^{-1}), respectively, for the period 2005–2014.

For the entire Kenai Range (subregions I-IV, Fig. 1), our results (-0.94 ± 0.12 m w.e. a^{-1}) are considerably more negative than the mass-balance rates of -0.06 ± 0.40 m w.e. a^{-1} from 1994/1996 to 1999/2001 reported by Arendt and others, 2009, and -0.45 ± 0.11 m w.e. a^{-1} between 1962 and 2006 found by Berthier and others, 2010, suggesting that glaciers mass loss in the Kenai Peninsula has strongly accelerated since at least the mid-2000s. These findings are in agreement with observed acceleration of glacier mass loss in Western Canada between the periods 2009–2018 and 2000–2009 (Menounos and others, 2019).

Our results are also more negative than regional-scale estimates in other regions in Alaska during similar periods, for example, on the Juneau Icefield and the Stikine Icefield (-0.68 ± 0.15 and -0.83 ± 0.12 m w.e. a^{-1}, respectively) over the period 2000–2016 (Berthier and others, 2018) and also averaged over all glaciers in Alaska and adjacent Yukon (-0.69 ± 0.18 m w.e. a^{-1}) for the period 2006–2015 (Hock and others, 2019).

4.5 Regional climate variability and trends

To investigate the causes of the accelerated glacier mass losses we analyzed air temperature and precipitation records on the Kenai Peninsula (Fig. 10, Table S7). Only four weather stations (A1, A2, A3, A4; Fig. 1) have longer than 30 years of largely uninterrupted observations through at least 2016, while data from the other five stations close to the ice masses (B1–B5, Fig. 1) are only available since 2005. All records show large interannual variation for both air temperature and precipitation (Fig. 10). We applied a moving *t*-test (Afifi and Azen, 1972; Fu and others, 1999) to the summer and winter temperature data to explore possible abrupt changes in temperature. Results indicate a significant change (at significance level $\alpha = 0.05$) in 2005 for all stations, except for summer temperature at A1 and A4, where the change occurred in 2002 and 1997, respectively (Fig. 11).

We calculate temperature trends for the period 2005–2016 for the five stations (B1–B5) that lack prior data and over the period 1986–2016 for the four stations (A1–A4) with longer records. Except for station A1 (1986–2016) and station B1 (2005–2016) linear warming trends in summer are not significant (Table S7). Three stations (B3, B4 and B5) show pronounced positive linear trends in winter temperature over the period 2005–2016, however, trends for the stations (A1–A4) going back to 1986 are not significant. In fact, mean summer and winter temperatures of the periods 1986–2005 and 2005–2016 are similar (Fig. 10). Precipitation variations are complex with both positive and negative trends, but only two stations (A1 and A4) have trends (negative) over the period 1986–2016 that are significant ($p < 0.05$, Table S7). Although decreasing precipitation is consistent with accelerated mass loss, the precipitation records are too short and scarce, especially at high elevation, to elucidate the role of precipitation in the observed glacier changes.

Overall, the large interannual variability and mostly short air temperature and precipitation records with largely insignificant changes of most of the investigated records hamper unambiguous attribution of the observed accelerated specific mass losses of the glaciers on the Kenai Peninsula during 2005–2014 compared to earlier periods covered in previous studies. In addition, changes in frontal ablation (calving and submarine melt) of tidewater glacier due to changes in ocean properties close to the calving fronts may also have contributed to accelerated mass loss, but their role remains unknown.

5. Conclusion

Four new glacier inventories of the Kenai peninsula glaciers in 1986, 1995, 2005 and 2016 were compiled from Landsat images indicating substantial area loss between 1986 and 2016 (543 ± 123 km^2, ~12%). Despite substantial scatter, relative area losses were generally considerably higher for smaller than larger glaciers, consistent with previous studies elsewhere. Geodetic mass-balance estimates derived from the IFSAR DEM in 2014 and DEMs generated from ASTER images in 2005 reveal substantial thinning and mass loss between 2005 and 2014 (-0.94 ± 0.12 m w.e. a^{-1}). Mass-balance rates vary strongly among the four subregions ranging from -0.69 ± 0.21 m w.e. a^{-1} (Sargent Icefield) to -1.63 ± 0.28 m w.e. a^{-1} (Grewing-Yalik glacier complex). These rates are considerably more negative than those found in previous studies for various periods between the early 1960s and late 1999s indicating strong acceleration of mass loss in this region. Thinning is generally most pronounced at lower elevations and both thinning and thickening is observed at higher elevations. The area-averaged specific mass-balance rate of the peninsula's lake-terminating glaciers is almost three times as negative than the rate of the tidewater glaciers and about twice as negative than the rate of the land-terminating glaciers.

Although the acquisition day of the year of the ASTER and IFSAR DEMs differed only by ~27 days, the calculated average region-wide mass-balance rate would have been underestimated by 0.09 m w.e. a^{-1} (~10%) if it was not corrected for, highlighting the importance of correcting for seasonal differences in acquisition dates in this case. Trends in available temperature and precipitation data on the Kenai Peninsula are mostly insignificant. Records are scarce and often short hampering unambiguous attribution of the acceleration in mass loss over the last decades. Further analysis is needed to determine the exact drivers of this acceleration. Process-based glacier modeling informed by the available data may help to attribute the observed acceleration in glacier mass loss in this region to their causes.

Supplementary material. The supplementary material for this article can be found at https://doi.org/10.1017/jog.2020.32.

Acknowledgements. Support for this work was provided by the Key Research Program of the Chinese Academy of Sciences (QYZDY-SSW-DQC02 and QYZDJ-SSW-DQC039), the China Scholarship Council, the Strategic Priority Research Program of the Chinese Academy of Sciences (XDA19070501), the National Natural Science Foundation of China (41721091) and the state Key Laboratory of Cryospheric Science (SKLCS-ZZ–2017). The study was partly developed during the visit of RY at the University of Alaska Fairbanks (UAF). We would like to thank Dr Martin Truffer, Dr Mark Fahnestock and other members of Glaciers Group in Geophysical Institute, UAF, for their kind support and valuable suggestions on this work. We also thank scientific editor Dr Shad O'Neel and the two anonymous reviewers for the constructive comments which led to the improvement of this manuscript.

References

Aðalgeirsdóttir G, Echelmeyer KA and Harrison WD (1998) Elevation and volume changes on the Harding Icefield, Alaska. *Journal of Glaciology* **44** (148), 570–582 doi: 10.3189/S0022143000002082.

Afifi AA and Azen SP (1972) *Statistical Analysis, A Computer Oriented Approach*. New York: Academic Press, Harcourt Brace Jovanonich Publishers.

Ahmad N and Rais S (1999) *Himalayan Glaciers*. New Dehli: APH Publishing Corporation.

Albert TH (2002) Evaluation of remote sensing techniques for ice-area classification applied to the Tropical Quelccaya Ice Cap, Peru. *Polar Geography* **26**(3), 210–226 doi: 10.1080/789610193.

Andreassen LM, Paul F, Kääb A and Hausberg JE (2008) Landsat-derived glacier inventory for Jotunheimen, Norway, and deduced glacier changes since the 1930s. *Cryosphere* **2**(2), 131–145 doi: 10.5194/tc-2-131-2008.

Arendt AA (2011) Assessing the Status of Alaska's glaciers. *Science* **332**(6033), 1044–1045 doi: 10.1126/science.1204400.

Arendt AA and 6 others (2013) Analysis of a GRACE global mascon solution for Gulf of Alaska glaciers. *Journal of Glaciology* **59**(217), 913–924 doi: 10.3189/2013JoG12J197.

Arendt AA, Echelmeyer KA, Harrison WD, Lingle CS and Valentine VB (2002) Rapid wastage of Alaska glaciers and their contribution to rising sea level. *Science (New York, N.Y.)* **297**(5580), 382–386 doi: 10.1126/science.1072497.

Arendt AA, Walsh J and Harrison W (2009) Changes of glaciers and climate in Northwestern North America during the late Twentieth Century. *Journal of Climate* **22**, 4117–4134, doi: 10.1175/2009JCLI2784.1.

Bert K, Blaskovich M, Reis JJ, Sanford M and Morgan K (2011) Fugro GeoSAR Airborne dual-band IFSAR DTM Processing. *ASPRS 2011 Annual Conference*.

Berthier E, Cabot V, Vincent C and Six D (2016) Decadal region-wide and glacier-wide mass balances derived from multi-temporal ASTER satellite digital elevation models. Validation over the Mont-Blanc area. *Frontiers in Earth Science* **4**, 63 doi: 10.3389/feart.2016.00063.

Berthier E, Larsen C, Durkin WJ, Willis MJ and Pritchard ME (2018) Brief communication: unabated wastage of the Juneau and Stikine icefields (southeast Alaska) in the early 21st century. *The Cryosphere* **12**(4), 1523–1530 doi: 10.5194/tc-12-1523-2018.

Berthier E, Scambos TA and Shuman CA (2012) Mass loss of Larsen B tributary glaciers (Antarctic Peninsula) unabated since 2002. *Geophysical Research Letters* **39**(13), L13501 doi: 10.1029/2012GL051755.

Berthier E, Schiefer E, Clarke GKC, Menounos B and Remy F (2010) Contribution of Alaskan glaciers to sea-level rise derived from satellite imagery. *Nature Geoscience* **3**(2), 92–95 doi: 10.1038/ngeo737.

Bolch T, Menounos B and Wheate R (2010) Landsat-based inventory of glaciers in western Canada, 1985–2005. *Remote Sensing of Environment* **114** (1), 127–137 doi: 10.1016./j.rse.2009.08. 015.

Bolch T, Pieczonka T and Benn DI (2011) Multi-decadal mass loss of glaciers in the Everest area (Nepal Himalaya) derived from stereo imagery. *Cryosphere* **5**(2), 349–358 doi: 10.5194/tc-5-349-2011.

Box JE and 6 others (2018) Global sea-level contribution from Arctic land ice: 1971–2017. *Environmental Research Letters* **13**(12), 125012 doi: 10.1088/1748-9326/aaf2ed.

Brun F, Berthier E, Wagnon P, Kääb A and Treichler D (2017) A spatially resolved estimate of high mountain Asia glacier mass balances from 2000 to 2016. *Nature Geoscience* **10**, 668 doi: 10.1038/ngeo2999.

Burns P and Nolin A (2014) Using atmospherically-corrected Landsat imagery to measure glacier area change in the Cordillera Blanca, Peru from 1987 to 2010. *Remote Sensing of Environment* **140**, 165–178 doi: 10.1016/j.rse.2013.08.026.

Das I, Hock R, Berthier E and Lingle CS (2014) 21st-century Increase in glacier mass loss in the Wrangell Mountains, Alaska, USA, from airborne laser altimetry and satellite stereo-imagery. *Journal of Glaciology* **60**(220), 283–293 doi: 10.3189/2014JoG13J119.

Davis CH and Poznyak VI (1993) The depth of penetration in 10 GHz. *IEEE Transactions on Geoscience and Remote Sensing* **31**(5), 1107–1111 doi: 10.1109/36.263784.

DeBeer C and Sharp M (2009) Topographic influences on recent changes of very small glaciers in the Monashee Mountains, British Columbia, Canada. *Journal of Glaciology* **55**(192), 691–700 doi: 10.3189/002214309789470851.

Dehecq A and 5 others (2016) Elevation changes inferred from TanDEM-X data over the Mont-Blanc Area: impact of the X-band interferometric bias. *IEEE Journal of Selected Topics in Applied Earth Observations and Remote Sensing* **9**(8), 3870–3882 doi: 10.1109/JSTARS.2016.2581482.

Dyurgerov MB and Meier MF (1997) Mass balance of mountain and subpolar glaciers: a new global assessment for 1961–1990. *Arctic and Alpine Research* **29**(4), 379–391 doi:10.2307/1551986.

Fischer M, Huss M and Hoelzle M (2015) Surface elevation and mass changes of all Swiss glaciers 1980–2010. *The Cryosphere* **9**(2), 525–540 doi: 10.5194/tc-9-525-2015.

Florentine C, Harper J, Fagre D, Moore J and Peitzsch E (2018) Local topography increasingly influences the mass balance of a retreating cirque glacier. *The Cryosphere* **12**(6), 2109–2122 doi: 10.5194/tc-12-2109-2018.

Fu C, Diaz HF, Dong D and Fletcher JO (1999) Changes in atmospheric circulation over northern hemisphere oceans associated with the rapid warming of the 1920s. *International Journal of Climatology* **19**(6), 581–606 doi: 10.1002/(SICI)1097-0088(199905)19:6<581::AID-JOC396>3.0.CO;2-P.

Gardelle J, Berthier E and Arnaud Y (2012) Impact of resolution and radar penetration on glacier elevation changes computed from DEM differencing. *Journal of Glaciology* **58**(208), 419–422 doi: 10.3189/2012JoG11J175.

Gardelle J, Berthier E, Arnaud Y and Kaab A (2013) Region-wide glacier mass balances over the Pamir-Karakoram-Himalaya during 1999–2011. *Cryosphere* **7**(6), 1885–1886 doi: 10.5194/tc-7-1885-2013.

Gardner AS and 15 others (2013) A reconciled estimate of glacier contributions to sea level rise: 2003 to 2009. *Science (New York, N.Y.)* **340**(6134), 852–857 doi: 10.1126/science.1234532.

Granshaw FD and Fountain AG (2006) Glacier change (1958–1998) in the North Cascades National Park Complex, Washington, USA. *Journal of Glaciology* **52**(177), 251–256 doi: 10.3189/172756506781828782.

Guo W and 10 others (2015) The second Chinese glacier inventory: data, methods and results. *Journal of Glaciology* **61**(226), 357–372 doi: 10.3189/2015JoG14J209.

Guo W, Liu S, Wei J and Bao W (2013) The 2008/09 surge of central Yulinchuan glacier, northern Tibetan Plateau, as monitored by remote sensing. *Annals of Glaciology* **54**(63), 299–310 doi: 10.3189/2013AoG63A495.

Gusmeroli A and 5 others (2013) Variable penetration depth of interferometric synthetic aperture radar signals on Alaska glaciers: a cold surface layer hypothesis. *Annals of Glaciology* **54**(64), 218–223 doi: 10.3189/2013AoG64A114.

Haeberli W and Hoelzle M (1995) Application of inventory data for estimating characteristics of and regional climate-change effects on mountain glaciers: a pilot study with the European Alps. *Annals of Glaciology* **21**, 206–212 doi: 10.1017/S0260305500015834.

Hall DK, Giffen BA and Chien JY (2005) Changes in the Harding Icefield and the Grewingk-Yalik Glacier Complex. In *Proceedings* of *62nd Eastern Snow Conference*, Waterloo, Ontario, Canada, June 7-10, 2005, 29–40.

Hall DK, Williams Jr RS and Bayr KJ (1992) Glacier recession in Iceland and Austria. *Eos, Transactions, American Geophysical Union* **73**(12), 129–141 doi: 10.1029/91EO00104.

Hock R (2019) High mountain areas. In Pörtner H-O Roberts DC Masson-Delmotte V Zhai P Tignor M Poloczanska E Mintenbeck K Alegría A Nicolai M Okem A Petzold J Rama B and Weyer NM eds. *In press*. 131–202. https://www.ipcc.ch/srocc/chapter/chapter-2/.

Huber J, McNabb R and Zemp M (2020) Elevation changes of West-Central Greenland glaciers from 1985 to 2012 from remote sensing. *Frontiers in Earth Science* **8**, 35 doi: 10.3389/feart.2020.00035.

Huss M (2013) Density assumptions for converting geodetic glacier volume change to mass change. *Cryosphere* **7**(3), 877–887 doi: 10.5194/tc-7-877-2013.

Johnson AJ, Larsen CF, Murphy N, Arendt AA and Zirnheld SL (2013) Mass balance in the Glacier Bay area of Alaska, USA, and British Columbia, Canada, 1995–2011, using airborne laser altimetry. *Journal of Glaciology* **59**(216), 632–648 doi: 10.3189/2013JoG12J101.

Kääb A, Paul F, Maisch M, Hoelzle M and Haeberli W (2002) The new remote sensing derived Swiss glacier inventory: II. First. *Annals of Glaciology* **34**, 362–366 doi: 10.3189/172756402781817473.

Kaser G and Osmaston H (2002) Tropical glaciers. Cambridge University Press. *UNESCO International Hydrological Series*, 207 pp.

Kienholz C and 5 others (2015) Derivation and analysis of a complete modern-date glacier inventory for Alaska and northwest Canada. *Journal of Glaciology* **61**(227), 403–420 doi: 10.3189/2015JoG14J230.

Koblet T and 6 others (2010) Reanalysis of multi-temporal aerial images of Storglaciären, Sweden (1959–99) – Part 1: determination of length, area, and volume changes. *The Cryosphere* **4**(3), 333–343 doi: 10.5194/tc-4-333-2010.

Lambrecht A, Mayer C, Wendt A, Floricioiu D and Völksen C (2018) Elevation change of Fedchenko Glacier, Pamir Mountains, from GNSS field measurements and TanDEM-X elevation models, with a focus on the upper glacier. *Journal of Glaciology* **64**(246), 637–648 doi: 10.1017/jog.2018.52.

Larsen CF and 5 others (2015) Surface melt dominates Alaska glacier mass balance. *Geophysical Research Letters* **42**(14), 5902–5908 doi: 10.1002/2015gl064349.

Le Bris R and Paul F (2015) Glacier-specific elevation changes in parts of western Alaska. *Annals of Glaciology* **56**(70), 184–192 doi: 10.3189/2015AoG70A227.

Le Bris R, Paul F, Frey H and Bolch T (2011) A new satellite-derived glacier inventory for western Alaska. *Annals of Glaciology* **52**(59), 135–143 doi: 10.3189/172756411799096303.

Li J and 7 others (2017) Early 21st century glacier thickness changes in the Central Tien Shan. *Remote Sensing of Environment* **192**, 12–29 doi: 10.1016/j.rse.2017.02.003.

Magruder LA, Webb CE, Urban TJ, Silverberg EC and Schutz BE (2007) ICESat altimetry data product verification at white sands space harbor. *Ieee Transactions on Geoscience and Remote Sensing* **45**(1), 147–155 doi: 10.1109/tgrs.2006.885070.

Maisch M, Haeberli W, Hoelzle M and Wenzel J. (1999) Occurrence of rocky and sedimentary glacier beds in the Swiss Alps as estimated from glacier-inventory data. In J. Kleman (Ed.), *Annals of Glaciology* **28**, 231–235 doi: 10.3189/172756499781821779.

Mätzler C and Schanda E (1984) Snow mapping with active microwave sensors. *International Journal of Remote Sensing* **5**(2), 409–422 doi: 10.1080/01431168408948816.

McGill R, Tukey JW and Larsen WA (1978) Variations of box plots. *The American Statistician* **32**(1), 12–16 doi: 10.1080/00031305.1978.10479236.

McNabb R, Nuth C, Kääb A and Girod L (2019) Sensitivity of glacier volume change estimation to DEM void interpolation. *The Cryosphere* **13**(3), 895–910 doi: 10.5194/tc-13-895-2019.

Meier MF and Dyurgerov MB (2002) Sea level changes: how Alaska affects the world. *Science (New York, N.Y.)* **297**(5580), 350–351 doi: 10.1126/science.1073591.

Melkonian AK, Willis MJ and Pritchard ME (2014) Satellite-derived volume loss rates and glacier speeds for the Juneau Icefield, Alaska. *Journal of Glaciology* **60**(222), 743–760 doi: 10.3189/2014JoG13J181.

Menounos B and 10 others (2019) Heterogeneous changes in Western North American glaciers linked to decadal variability in zonal wind strength. *Geophysical Research Letters* **46**(1), 200–209 doi: 10.1029/2018gl080942.

Millan R, Dehecq A, Trouve E, Gourmelen N and Berthier E. (2015) Elevation changes and X-band ice and snow penetration inferred from TanDEM-X data of the Mont-Blanc area. Paper presented at *the 2015 8th International Workshop on the Analysis of Multitemporal Remote Sensing Images* (Multi-Temp).

Molnia BF (2007) Late nineteenth to early twenty-first century behavior of Alaskan glaciers as indicators of changing regional climate. *Global and Planetary Change* **56**(1–2), 23–56 doi: 10.1016/j.gloplacha.2006.07.011.

Moore GWK, Holdsworth G and Alverson K (2002) Climate change in the North Pacific region over the past three centuries. *Nature* **420**(6914), 401–403 doi: 10.1038/nature01229.

NASA LP DAAC (2015) ASTER Level 1 Precision Terrain Corrected Registered At-Sensor Radiance.Version 3. *NASA EOSDIS Land Processes DAAC, USGS Earth Resources Observation and Science (EROS) Center, Sioux Falls, South Dakota*. Available at https://lpdaac.usgs.gov (Accessed 1 June 2017).

Nuth C and Kääb A (2011) Co-registration and bias corrections of satellite elevation data sets for quantifying glacier thickness change. *Cryosphere* **5**(1), 271–290 doi: 10.5194/tc-5-271-2011.

O'Neel S and 8 others (2019) Reanalysis of the US geological survey benchmark glaciers: long-term insight into climate forcing of glacier mass balance. *Journal of Glaciology* **65**(253), 850–866 doi: 10.1017/jog.2019.66.

O'Neel S, Hood E, Arendt A and Sass L (2014) Assessing streamflow sensitivity to variations in glacier mass balance. *Climatic Change* **123**(2), 329–341 doi: 10.1007/s10584-013-1042-7.

Pan BT and 7 others (2012) Glacier changes from 1966–2009 in the Gongga Mountains, on the south-eastern margin of the Qinghai-Tibetan Plateau and their climatic forcing. *Cryosphere* **6**(5), 1087–1101 doi: 10.5194/tc-6-1087-2012.

Paul F (2000) Evaluation of different methods for glacier mapping using Landsat TM. *Paper presented at the Proceedings*, EARSeL-SIG Workshop.

Paul F (2002) Changes in glacier area in Tyrol, Austria, between 1969 and 1992 derived from Landsat 5 thematic mapper and Austrian glacier inventory data. *International Journal of Remote Sensing* **23**(4), 787–799 doi: 10.1080/01431160110070708.

Paul F and Andreassen LM (2009) A new glacier inventory for the Svartisen region, Norway, from Landsat ETM plus data: challenges and change assessment. *Journal of Glaciology* **55**(192), 607–618 doi: 10.3189/002214309789471003.

Paul F, Frey H and Le Bris R (2011) A new glacier inventory for the European Alps from Landsat TM scenes of 2003: challenges and results. *Annals of Glaciology* **52**(59), 144–152 doi: 10.3189/172756411799096295.

Paul F and Kääb A (2005) Perspectives on the production of a glacier inventory from multispectral satellite data in Arctic Canada: Cumberland Peninsula, Baffin Island. In J. Dowdeswell & I. C. Willis (Eds.), *Annals of Glaciology* **42**, 59–66 doi: 10.3189/172756405781813087.

Paul F and Svoboda F (2009) A new glacier inventory on southern Baffin Island, Canada, from ASTER data: II. Data analysis, glacier change and applications. *Annals of Glaciology* **50**(53), 22–31 doi: 10.3189/172756410790595921.

Pelto BM, Menounos B and Marshall SJ (2019) Multi-year evaluation of airborne geodetic surveys to estimate seasonal mass balance, Columbia and Rocky Mountains, Canada. *The Cryosphere* **13**(6), 1709–1727 doi: 10.5194/tc-13-1709-2019.

Pfeffer WT and 76 others (2014) The Randolph Glacier Inventory: a globally complete inventory of glaciers. *Journal of Glaciology* **60**(221), 537–552 doi: 10.3189/2014JoG13J176.

Pieczonka T and Bolch T (2015) Region-wide glacier mass budgets and area changes for the Central Tien Shan between ~1975 and 1999 using Hexagon KH-9 imagery. *Global and Planetary Change* **128**, 1–13 doi: 10.1016/j.gloplacha.2014.11.014.

Racoviteanu AE, Arnaud Y, Williams MW and Manley WF (2015) Spatial patterns in glacier characteristics and area changes from 1962 to 2006 in the Kanchenjunga-Sikkim area, eastern Himalaya. *Cryosphere* **9**(2), 505–523 doi: 10.5194/tc-9-505-2015.

Racoviteanu AE, Arnaud Y, Williams MW and Ordonez J (2008*a*) Decadal changes in glacier parameters in the Cordillera Blanca, Peru, derived from remote sensing. *Journal of Glaciology* **54**(186), 499–510 doi: 10.3189/002214308785836922.

Racoviteanu AE, Williams MW and Barry RG (2008*b*) Optical remote sensing of glacier characteristics: a review with focus on the Himalaya. *Sensors* **8**(5), 3355–3383 doi: 10.3390/s8053355.

Raup B and 11 others (2007) Remote sensing and GIS technology in the Global Land Ice Measurements from Space (GLIMS) project. *Computers & Geosciences* **33**(1), 104–125 doi: 10.1016/j.cageo.2006.05.015.

RGI Consortium (2017) Randolph Glacier Inventory – A Dataset of Global Glacier Outlines: Version 6.0: Technical Report, *Global Land Ice Measurements from Space, Colorado, USA. Digital Media* doi: 10.7265/N5-RGI-60.

Rignot E, Echelmeyer K and Krabill W (2001) Penetration depth of interferometric synthetic-aperture radar signals in snow and ice. *Geophysical Research Letters* **28**(18), 3501–3504 doi: 10.1029/2000gl012484.

Rivera A, Bown F, Casassa G, Acuna C and Clavero J (2005) Glacier shrinkage and negative mass balance in the Chilean Lake District (40 degrees S). *Hydrological Sciences Journal-Journal Des Sciences Hydrologiques* **50**(6), 963–974 doi: 10.1623/hysj.2005.50.6.963.

Rolstad C, Haug T and Denby B (2009) Spatially integrated geodetic glacier mass balance and its uncertainty based on geostatistical analysis: application to the western Svartisen ice cap, Norway. *Journal of Glaciology* **55**(192), 666–680 doi: 10.3189/002214309789470950.

Round V, Leinss S, Huss M, Haemmig C and Hajnsek I (2017) Surge dynamics and lake outbursts of Kyagar Glacier, Karakoram. *The Cryosphere* **11**(2), 723–739 doi: 10.5194/tc-11-723-2017.

Salerno F, Buraschi E, Bruccoleri G, Tartari G and Smiraglia C (2008) Glacier surface-area changes in Sagarmatha national park, Nepal, in the second half of the 20th century, by comparison of historical maps. *Journal of Glaciology* **54**(187), 738–752 doi: 10.3189/002214308786570926.

Serandrei Barbero R, Rabagliati R, Bianghi E and Rampini A (1999) Glacial retreat in the 1980s in the Breonie, Aurine and Pusteresi groups (eastern Alps, Italy) in Landsat TM images. *Hydrological Sciences Journal-Journal Des Sciences Hydrologiques* **44**(2), 279–296 doi: 10.1080/02626669909492222.

Surdyk S (2002) Using microwave brightness temperature to detect short-term surface air temperature changes in Antarctica: an analytical approach. *Remote Sensing of Environment* **80**(2), 256–271 doi: 10.1016/s0034-4257(01)00308-x.

Tielidze LG and Wheate RD (2018) The greater Caucasus glacier inventory (Russia, Georgia and Azerbaijan). *Cryosphere* **12**(1), 81–94 doi: 10.5194/tc-12-81-2018.

US Geological Survey, Gap Analysis Program (GAP) (2011) National Land Cover, Version 2.

Van Beusekom AE, O'Neel S, March R, Sass L and Cox L (2010) Re-analysis of Alaskan Benchmark Glacier mass-balance data using the index method. *Scientific investigations Report*, U.S. Geological Survey.

VanLooy J, Forster R and Ford A (2006) Accelerating thinning of Kenai Peninsula glaciers, Alaska. *Geophysical Research Letters* **33**(21), L21307 doi: 10.1029/2006gl028060.

https://doi.org/10.1017/jog.2020.32 Published online by Cambridge University Press

Wastlhuber R, Hock R, Kienholz C and Braun M (2017) Glacier changes in the Susitna Basin, Alaska, USA, (1951–2015) using GIS and remote sensing methods. *Remote Sensing* **9**(5), 478 doi: 10.3390/rs9050478.

Wiles GC and Calkin PE (1992) Reconstruction of a debris-slide-initiated flood in the southern Kenai Mountains, Alaska. *Geomorphology* **5**(1992), 535–546.

Wouters B, Gardner AS and Moholdt G (2019) Global Glacier Mass Loss During the GRACE Satellite Mission (2002–2016). *Frontiers of Earth Science* **7**, 96 doi: 10.3389/feart.2019.00096.

Zemp M and 16 others (2013) Reanalysing glacier mass balance measurement series. *The Cryosphere* **7**(4), 1227–1245 doi: 10.5194/tc-7-1227-2013.

Zemp M and 14 others (2019) Global glacier mass changes and their contributions to sea-level rise from 1961 to 2016. *Nature* **568**(7752), 382–386 doi: 10.1038/s41586-019-1071-0.

Zwally HJ, Schutz R, Hancock D and Dimarzio J (2014) GLAS/ICEsat L2 Global Land Surface Altimetry Data (HDF5), Version 34. 59°N to 61°N, 148°W to 151°W.

https://doi.org/10.1017/jog.2020.32 Published online by Cambridge University Press